

As a library, NLM provides access to scientific literature. Inclusion in an NLM database does not imply endorsement of, or agreement with, the contents by NLM or the National Institutes of Health.

Learn more: [PMC Disclaimer](#) | [PMC Copyright Notice](#)

## Author Manuscript

Peer reviewed and accepted for publication by a journal



[Sci Transl Med.](#) Author manuscript; available in PMC 2013 Aug 15.

PMCID: PMC3551275

Published in final edited form as:

NIHMSID: NIHMS432693

[Sci Transl Med.](#) 2012 Aug 15; 4(147): 147ra111.

PMID: [22896675](#)

doi: [10.1126/scitranslmed.3003748](#)

# A Paravascular Pathway Facilitates CSF Flow Through the Brain Parenchyma and the Clearance of Interstitial Solutes, Including Amyloid $\beta$

[Jeffrey J. Iliff](#)<sup>1,\*</sup>, [Minghuan Wang](#)<sup>1,2</sup>, [Yonghong Liao](#)<sup>1</sup>, [Benjamin A. Plogg](#)<sup>1</sup>, [Weiguo Peng](#)<sup>1</sup>, [Georg A. Gundersen](#)<sup>3,4</sup>, [Helene Benveniste](#)<sup>5,6</sup>, [G. Edward Vates](#)<sup>1</sup>, [Rashid Deane](#)<sup>1</sup>, [Steven A. Goldman](#)<sup>1,7</sup>, [Erlend A. Nagelhus](#)<sup>3,4</sup> and [Maiken Nedergaard](#)<sup>1,\*</sup>

## Abstract

Because it lacks a lymphatic circulation, the brain must clear extracellular proteins by an alternative mechanism. The cerebrospinal fluid (CSF) functions as a sink for brain extracellular solutes, but it is not clear how solutes from the brain interstitium move from the parenchyma to the CSF. We demonstrate that a substantial portion of subarachnoid CSF cycles through the brain interstitial space. On the basis of in vivo two-photon imaging of small fluorescent tracers, we showed that CSF enters the parenchyma along paravascular spaces that surround penetrating arteries and that brain interstitial fluid is cleared along paravenous drainage pathways. Animals lacking the water channel aquaporin-4 (AQP4) in astrocytes exhibit slowed CSF influx through this system and a ~70% reduction in interstitial solute clearance, suggesting that the bulk fluid flow between these anatomical influx and efflux routes is supported by astrocytic water transport. Fluorescent-tagged amyloid  $\beta$ , a peptide thought to be pathogenic in Alzheimer's disease, was transported along this route, and deletion of the *Aqp4* gene suppressed the clearance of soluble amyloid  $\beta$ , suggesting that this pathway may remove amyloid  $\beta$  from the central nervous system. Clearance through paravenous flow may also regulate extracellular levels of proteins involved with neurodegenerative conditions, its impairment perhaps contributing to the mis-accumulation of soluble proteins.



## INTRODUCTION

The lymphatic vasculature represents a second circulation, parallel to the blood vasculature, that accounts for the clearance of interstitial fluid (ISF) with its constituent proteins and other solutes not absorbed across postcapillary venules (1, 2). In most vascularized tissues, the lymphatic system is critical

to both hydrostatic and homeostatic maintenance. Yet, the brain does not have histologically identifiable lymphatic vessels and thus lacks the discrete pathways for interstitial solute and fluid clearance present in other peripheral tissues (3–5). This is surprising, because the high metabolic rate and exquisite sensitivity of neurons and glia to alterations in their extracellular environment suggest a need for rapid clearance of ISF and solutes.

The cerebrospinal fluid (CSF) of the central nervous system (CNS) has been thought to play a role in solute clearance from the brain (6). CSF formed in the choroid plexi flows through the cerebral ventricles and the subarachnoid space to its ultimate sites of reabsorption into the bloodstream via arachnoid villi of the dural sinuses, along cranial nerve sheaths or through the nasal lymphatics (3, 7, 8). Interstitial solutes have been thought to be cleared to the CSF by the convective bulk flow of ISF, which courses diffusely through brain tissue, rather than through an anatomically or functionally discrete structure (3, 4, 9). Here, we have used in vivo two-photon imaging and other techniques to investigate the flow of subarachnoid CSF into and through the brain interstitium.

## RESULTS

---

### Ventricular CSF minimally enters the brain parenchyma

We first evaluated whether CSF enters the brain from the ventricular compartment by infusing fluorescent tracers of differing molecular weights into the lateral ventricle of anesthetized mice (Fig. 1A). After 30 min of continuous infusion, we assessed the movement of tracers [Alexa Fluor 594 hydrazide (A594): molecular size, 759 daltons; Texas Red–dextran-3 (TR-d3): molecular size, 3 kD; fluorescein isothiocyanate–dextran-2000 (FITC-d2000): molecular size, 2000 kD] into the brain parenchyma ex vivo by fluorescence imaging of fixed vibratome slices. Small amounts of A594 and TR-d3 crossed the ependyma of the lateral and third ventricles (Fig. 1, B, C, E, and F). However, the tracer was not observed at sites remote from the immediate periventricular region (Fig. 1, D and G).

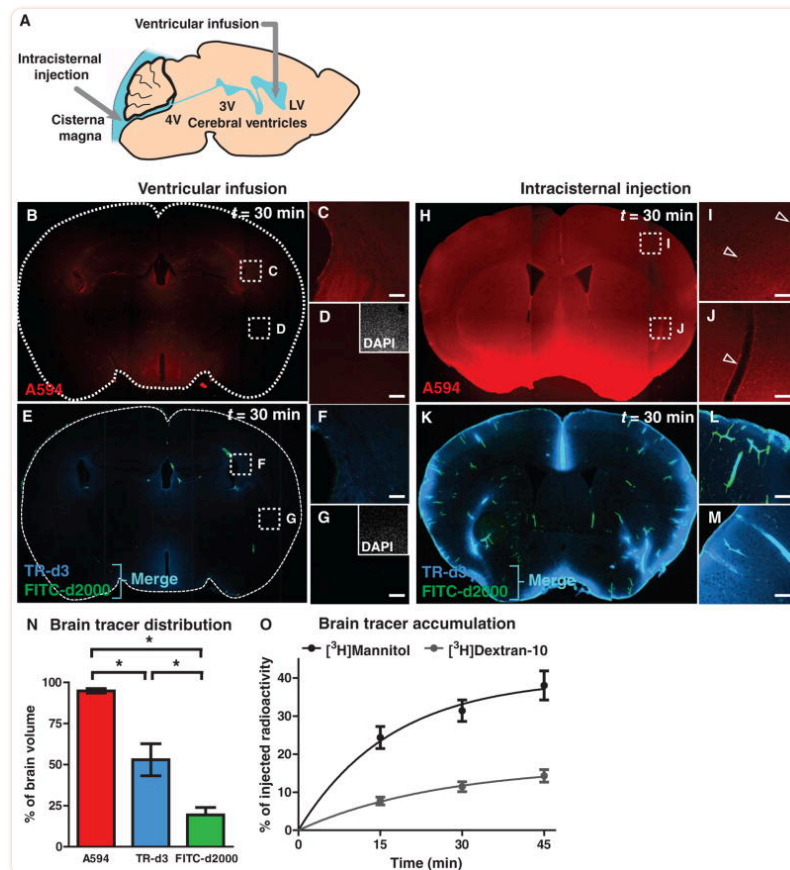


**Fig. 1**

Distribution of subarachnoid CSF into the brain parenchyma. (A) The movement of ventricular and subarachnoid CSF into the brain parenchyma was evaluated after infusion of fluorescent tracer into the lateral ventricle (LV) or cisterna magna. (B to G) After 30 min of intraventricular infusion, small- (A594; molecular size, 759 daltons; red), moderate- (TR-d3; molecular size, 3 kD; blue), and large-molecular weight (FITC-d2000; molecular size, 2000 kD; green) tracer movement into the brain parenchyma was evaluated. 3V, third ventricle; 4V, fourth ventricle. (D and G) Absence of tracer in tissue remote from the periventricular space. Insets, 4',6-diamidino-2-phenylindole (DAPI) labeling in the same fields of view. (H to J) Small-molecular weight tracer permeation 30 min after intracisternal injection. Arrowheads, low-level paravascular accumulation. (K to M) Distribution of intracisternally injected TR-d3 (dark blue) and FITC-d2000 (green). Merge (light blue) indicates colocalization of TR-d3 and FITC-d2000. (N) Distributions of intracisternal fluorescent tracers, quantified as a percentage of total brain volume (integrated slice areas). A594 occupied the greatest proportion of brain tissue. TR-d3 exhibited an intermediate distribution, whereas FITC-d2000 was highly restricted ( $n = 3$ ,  $*P < 0.05$ ). (O) Accumulation of radiotracer within the brain after intracisternal injection of [<sup>3</sup>H]mannitol (molecular size, 182 daltons) or [<sup>3</sup>H]dextran-10 (molecular size, 10 kD). Compared to [<sup>3</sup>H]mannitol, [<sup>3</sup>H]dextran-10 accumulation in the brain was significantly slower ( $n = 6$  per time point,  $*P < 0.0001$ ). Scale bars, 100  $\mu$ m.

## Subarachnoid CSF rapidly enters the brain parenchyma

We next evaluated whether CSF from the subarachnoid compartment enters the brain parenchyma by injecting both fluorescent and radiolabeled tracers into the cisterna magna (Fig. 1A). Thirty minutes after injection, fluorescent tracer distribution differed radically from the pattern observed after the tracers were injected into the ventricles (Fig. 1, H and K, compare to Fig. 1, B and E). Large-molecular weight FITC-d2000 (molecular size, 2000 kD) entered the brain along paravascular spaces, was confined there,

and did not enter the surrounding interstitial space ([Fig. 1, K and L](#)). TR-d3 (molecular size, 3 kD) concentrated in the paravascular spaces but also entered the interstitium both from the paravascular space (K and L) and from the pial surface (M) ([Fig. 1, K and L](#)). TR-d3 was more widely distributed than FITC-d2000, which is mainly localized paravascularly. The lower-molecular weight A594 (molecular size, 759 daltons) moved quickly throughout the brain interstitium, and only small amounts concentrated within paravascular spaces ([Fig. 1, H and J](#)). Both A594 and TR-d3 moved slowly and uniformly into the brain from the pial surface ([Fig. 1, H, K, and M](#)). We then quantified parenchymal distribution of tracers of different molecular weights by image analysis ([fig. S1](#)). Whereas A594 permeated virtually the entire brain volume within 30 min of injection, penetration of the higher-molecular weight tracers proved more restricted ([Fig. 1N](#)).

These findings were confirmed by intracisternal radiotracer injection. Within 45 min of injection, ~40% of injected [ $^3\text{H}$ ]mannitol (molecular size, 182 daltons; [fig. S2](#)) was detectable in the brain ([Fig. 1O](#)). A larger tracer ([ $^3\text{H}$ ]dextran-10; molecular size, 10 kD) accumulated in the brain more slowly ([Fig. 1O](#)). Because water has a 10-fold lower molecular weight than mannitol, the CSF flux reflected by [ $^3\text{H}$ ]mannitol accumulation (~40% of total subarachnoid CSF) likely underestimates the true movement of CSF into the brain parenchyma. Previous studies that have evaluated the penetration of subarachnoid CSF into the brain have used tracers such as inulin (molecular size, ~5 kD), albumin (molecular size, 66 kD), and dextrans (molecular size, 3 to 2000 kD) ([10](#), [11](#)). Our findings show that higher-molecular weight tracers are preferentially excluded from the brain parenchyma, suggesting that previous studies may have systematically underestimated “retrograde” subarachnoid CSF flow into the brain by basing their analyses on larger tracers.

### In vivo imaging reveals paravascular CSF influx

We next used two-photon laser scanning microscopy to visualize in real time the routes and kinetics of subarachnoid CSF influx into the brain parenchyma. By imaging through a closed cranial window in anesthetized mice ([Fig. 2A](#)), we visualized the movement of intracisternally injected fluorescent dextrans into the cerebral cortex. The cerebral vasculature was labeled with blood-brain barrier (BBB)-impermeant fluorescent dextran (CB-d10) (intravenously), and penetrating arteries and veins were identified morphologically ([Fig. 2B](#)).

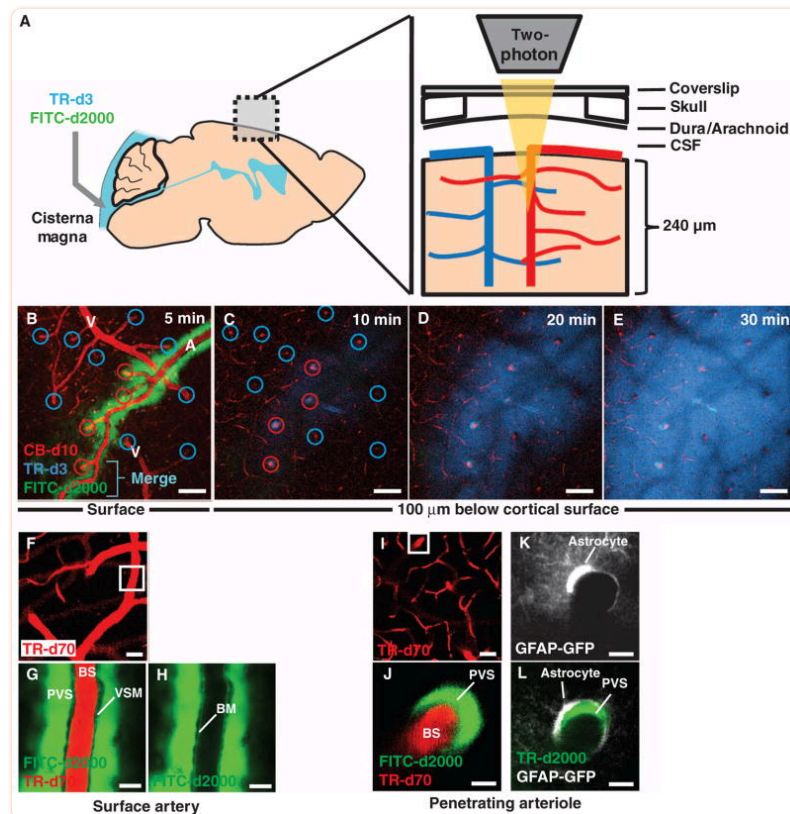


[Fig. 2](#)

In vivo two-photon imaging of para-arterial CSF flux into the mouse cortex. The influx into the cerebral cortex of tracers injected intracisternally into the subarachnoid CSF was assessed in vivo by two-photon imaging through a closed cranial window. (A) Schematic of imaging setup. Imaging was conducted between 0 and 240  $\mu\text{m}$  below the cortical surface at 1-min intervals. (B) The cerebral vasculature was visualized with intra-arterial CB-d10, and arteries (A) and veins (V) were identified morphologically. Immediately after intracisternal injection, CSF tracer moved along the outside of cerebral surface arteries, but not veins. Red circles, arterioles; blue circles, venules. (C to E) Over time, tracer moved rapidly into the brain along penetrating arterioles, but not venules. The small-molecular weight tracer (TR-d3, dark blue) moved readily into the interstitium, whereas the large-molecular weight tracer (FITC-d2000, green) was confined to the paravascular space. Merge (light blue) indicates colocalization of TR-d3 and FITC-d2000. (F to H) Along the cortical surface arteries, the large-molecular weight tracer (FITC-d2000) was present in the paravascular space (PVS) immediately surrounding the arterial vascular smooth muscle cells (VSM). The bloodstream (BS) is defined by intravenously injected TR-d70. Low-level labeling of the basement membrane (BM) shows that a small proportion of CSF tracer moves along the basement membrane. (I and J) Intracisternally injected large-molecular weight tracer (FITC-d2000) entered the brain along paravascular spaces surrounding penetrating arterioles (TR-d70). (K and L) Glial fibrillary acidic protein (GFAP)-positive astrocytes in transgenic mice expressing a GFAP-GFP (green fluorescent protein) reporter. The paravascular space containing TR-d2000 is bounded by perivascular astrocytic endfeet (white). Scale bars, 100  $\mu\text{m}$  [(B) to (E)], 20  $\mu\text{m}$  [(F) to (I)], and 5  $\mu\text{m}$  [(J) to (L)].

After injection, the tracers rapidly entered the brain along the outside of cortical surface arteries and penetrating arterioles ([Fig. 2, B and C](#), and [fig. S3](#)) through a pathway immediately surrounding the vascular smooth muscle cells ([Figs. 2, F to J](#), and [3, C and E](#)) and bounded by perivascular astrocytic endfeet ([Figs. 2, K and L](#), and [4, B to D](#)). This para-arterial CSF movement was seen as FITC-d40 (molecular size, 40 kD) influx more than ~35 min after intracisternal injection at the cortical surface, 60 and 120  $\mu\text{m}$  below the cortical surface ([movie S1](#)). Rapid tracer movement along the margins of sur-



face arteries, rather than through the subarachnoid CSF, is consistent with the presence of paravascular sheaths surrounding cerebral surface arteries, as described by Weller (12). These paravascular spaces are continuous with the subarachnoid space yet provide distinct channels for the rapid para-arterial bulk flow of CSF into the parenchyma, driven by arterial pulsation (13–15).

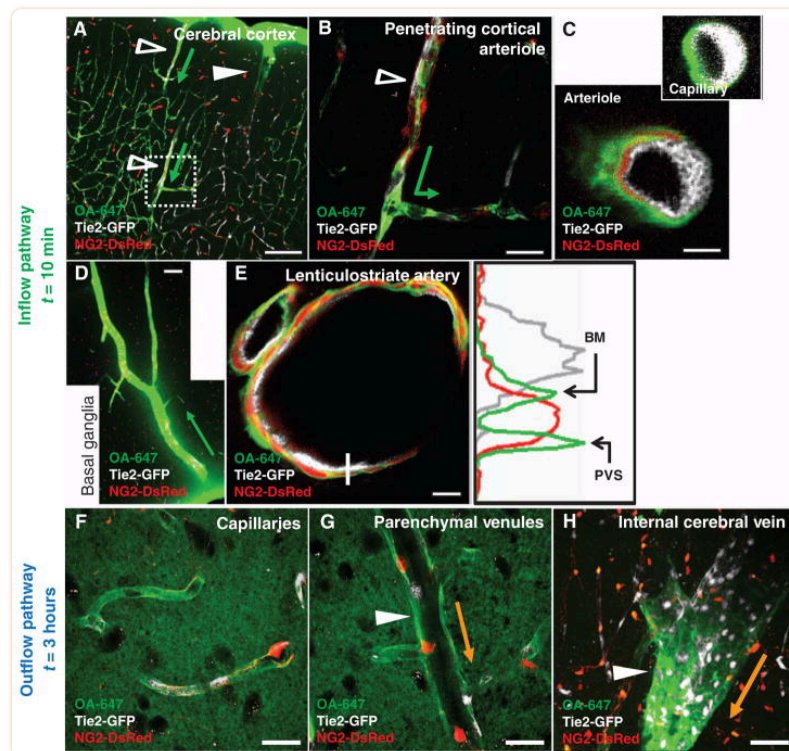


**Fig. 3**

CSF enters and is cleared from the brain interstitium along paravascular pathways. To evaluate the pathways of subarachnoid CSF flux into the brain parenchyma, we injected fluorescent tracer intracisternally into Tie2-GFP:NG2-DsRed double reporter mice, allowing arteries and veins to be directly distinguished. (A and B) Intracisternally injected OA-647 enters (green arrows depict tracer entry) the cerebral cortex along penetrating arterioles (Tie2-GFP<sup>+</sup>/NG2-DsRed<sup>+</sup> vessels, empty arrowheads), not along ascending veins (Tie2-GFP<sup>+</sup>/NG2-DsRed<sup>-</sup> vessels, filled arrowheads). (C) CSF tracer moves along both paravascular space (PVS) and the basement membrane (BM) between the vascular endothelial and the smooth muscle cell layers. Tracer movement along capillaries proceeds along the basal lamina. (D) Large amounts of tracer are observed in the basal ganglia and thalamus, entering along large ventral perforating arteries. (E) Detailed tracer distribution around lenticulostriate artery. Plot shows intensity projection along white line. Green, tracer; gray, endothelial GFP; red, vascular smooth muscle. (F to H) At longer time points (>1 hour compared to 0 to 30 min for tracer influx), OA-647 (molecular size, 45 kD) entered the interstitial space and accumulated primarily along capillaries (F) and parenchymal venules (G). Accumulation was greatest along medial interior cerebral veins and ventral-lateral caudal rhinal veins (H). Orange arrows in (G) to (H) depict the observed route of interstitial tracer clearance. Scale bars, 100  $\mu$ m [(A) and (D)], 50  $\mu$ m (H), 20  $\mu$ m [(B), (F), and (G)], and 4  $\mu$ m [(C) and (E)].

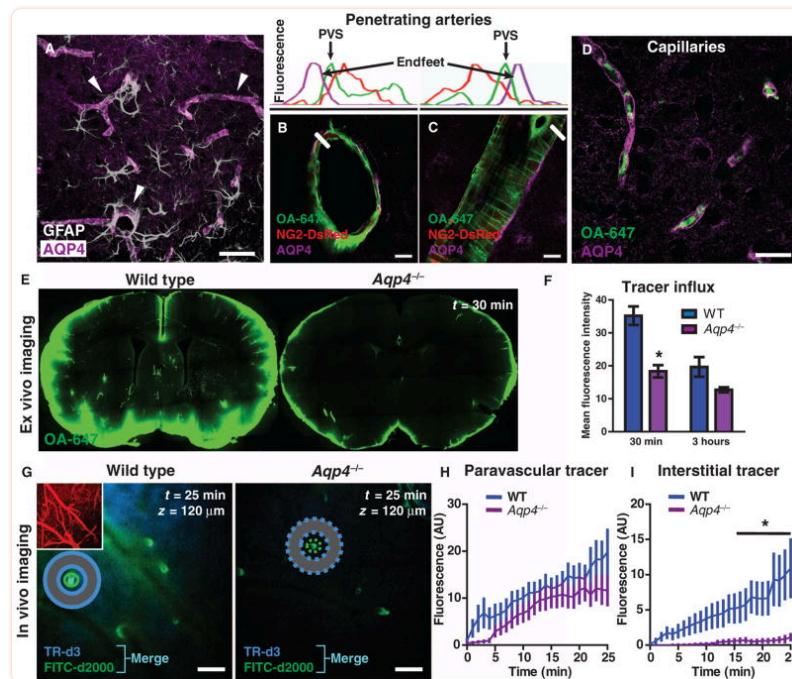


Fig. 4

Paravascular AQP4 facilitates CSF flux through the brain interstitium. (A) AQP4 (purple) is specifically expressed in brain astrocytes (white), where localization is highly polarized to perivascular endfeet (arrowheads). (B and C) AQP4-positive perivascular astrocytic endfeet immediately surround the para-arterial CSF influx pathway. Plots depict fluorescence intensity projections from (B) and (C), indicated by white rectangles. Tracer (green) is localized within the paravascular space (PVS), between the vascular smooth muscle (red) and the astrocytic endfeet (purple). (D) Tracer movement along the capillary basal lamina (green) is bounded by perivascular AQP4-positive endfeet (purple). (E and F) The contribution of AQP4-mediated fluid flux to the movement of subarachnoid CSF into and through the brain parenchyma was evaluated ex vivo. When tracer labeling was quantified, the movement of intracisternally injected tracer into the brain was significantly reduced in *Aqp4*-null mice compared to wild-type (WT) controls 30 min after injection ( $n = 4$  to 5 per time point,  $*P < 0.05$ ). (G) The influx of small- (TR-d3) (dark blue) and large-molecular weight (FITC-d2000) (green) intracisternal tracers into the cortex was evaluated in vivo. The cerebral vasculature was visualized with intra-arterial CB-d10 (inset). Merge (light blue) indicates colocalization of TR-d3 and FITC-d2000. (H) The movement of large-molecular weight tracer (green) along para-arterial spaces [as measured by the mean fluorescence intensity in green circle region of interests (ROIs)] was not significantly altered in *Aqp4*-null versus WT control animals. (I) The movement of small-molecular weight tracer into the interstitium surrounding penetrating arterioles (as measured by the mean fluorescence intensity in the blue donut ROIs) was abolished in *Aqp4*-null compared to WT controls ( $n = 6$  per group,  $*P < 0.01$ ), demonstrating that *Aqp4* gene deletion affects the movement of intracisternally injected tracer through the cortical parenchyma. AU, arbitrary units. Scale bars, 100  $\mu\text{m}$  (G), 40  $\mu\text{m}$  (A), 20  $\mu\text{m}$  (D), and 10  $\mu\text{m}$  [(B) and (C)].

When TR-d3 (molecular size, 3 kD) and FITC-d2000 (molecular size, 2000 kD) were injected, both rapidly entered the paravascular spaces along penetrating cortical arteries, despite large differences in their respective molecular weights (fig. S3, C and D). This suggested that their transit occurs via bulk CSF flow through the paravascular spaces (4, 16). In contrast, movement from the paravascular spaces into the surrounding tissue differed between FITC-d2000 and TR-d3. TR-d3 readily entered the interstitium, whereas the larger FITC-d2000 remained confined to the paravascular space (Fig. 2, C to E, and fig. S3, B to D). A recent study demonstrated that astrocytic endfeet cover most of the surface area of

the murine cerebral microcirculation so that access to the parenchyma is provided only by ~20-nm clefts between overlapping endfeet (17). This suggests that perivascular astrocytic endfeet may serve a sieving function, thereby accounting for the size dependence of paravascular solute entry into the interstitium. Although water and small solutes may freely enter the brain interstitium from the paravascular spaces by bulk flow, large-molecular weight solutes [FITC-d2000; diameter of hydration ( $d_H$ ) >32 nm (9)] are excluded, whereas smaller solutes [for example, ovalbumin and TR-d3;  $d_H$  = 2 to 3 nm and 6.1 nm, respectively (9)] pass the endfeet in a size- and structure-dependent manner (Fig. 2E and fig. S3, B to D).

### Paravascular CSF influx and clearance occur throughout the brain

In vivo imaging demonstrated para-arterial influx of subarachnoid CSF into the cortex. However, because two-photon imaging cannot image tracer fluxes through deeper brain structures, we next used an ex vivo approach to map paravascular CSF influx and clearance throughout the brain. The distribution of the moderate molecular weight tracer ovalbumin-conjugated Alexa Fluor 647 (OA-647; molecular size, 45 kD) was analyzed in fixed vibratome sections of the Tie2-GFP:NG2-DsRed double-transgenic reporter mouse, in which we could easily distinguish arteries from veins (fig. S4A). Immediately after intracisternal injection, the tracer moved rapidly inward along penetrating arteries and arterioles to reach the terminal capillary beds throughout the brain (Fig. 3A), with the largest influxes occurring along large ventral perforating arteries of the basal ganglia and thalamus (Fig. 3D and fig. S4, C to E). The tracer was not observed around veins at early time points (<10 min after injection). At longer time points (>1 hour), tracers that had been injected intracisternally accumulated along capillaries and parenchymal venules (Fig. 3, F and G). The tracer exited the brain primarily along two paravenous routes: the medial internal cerebral veins and the lateral-ventral caudal rhinal veins (Fig. 3H).

Intraparenchymal tracer injected directly into the cortex, striatum, or thalamus was cleared along the same common anatomical pathways, traveling either posterior-medially toward the internal cerebral veins or posterior-lateral-ventrally along the external capsule until its exit from the parenchyma along the caudal rhinal veins (fig. S5, A to E). These results demonstrated that ISF and CSF that is moving through the brain parenchyma are cleared along the same paravenous drainage pathways.

### Astroglial water transport supports CSF flux into the parenchyma

The localization of astroglial aquaporin-4 (AQP4) water channel is highly polarized to perivascular endfeet (Fig. 4A) that bound the para-arterial CSF influx and the paravenous ISF clearance pathways (Fig. 4, B to D). We propose that these astrocytic water channels provide low-resistance pathways for fluid movement between these paravascular spaces and the interstitium, linking paravascular and interstitial bulk flow and maintaining convective currents (3, 9) that drive the clearance of interstitial solutes from the brain parenchyma. To test this, we determined whether increasing parenchymal resistance to fluid flux by the global knockout of the *Aqp4* gene altered CSF flux through the interstitium. When CSF tracer influx was imaged ex vivo, tracer movement into the brain parenchyma was markedly reduced in *Aqp4*-null compared to wild-type control mice (Fig. 4, E and F, and fig. S6, A and B). In vivo imaging confirmed these findings. After intracisternal injection, FITC-d2000 movement along the para-arteriolar inflow path was not significantly slowed in *Aqp4*-null mice (Fig. 4, G and H), demonstrating that bulk flow through the proximal segment of the para-arterial influx pathway (the Virchow-Robin space) was not compromised by *Aqp4* deletion. In contrast, TR-d3 movement from the paravascular space into the surrounding interstitium was effectively abolished in *Aqp4*-null mice (Fig. 4, G and I). We confirmed that in *Aqp4*-null mice, the paravascular spaces surrounding penetrating cortical arteri-



oles were ultrastructurally normal through the depth of the cortex ([fig. S6, C to E](#)) and that intracisternally injected FITC-d40 was detectable within the paravascular space of *Aqp4*-null as well as in that of wild-type mice by electron microscopy ([fig. S6, C and D](#)).

We surmised that differences in AQP4 expression may contribute to the polarization of bulk flow along these para-arterial CSF influx and paravenous ISF clearance pathways. We therefore assessed AQP4 immunoreactivity in NG2-DsRed animals (in which veins and arteries can be distinguished) to define the relative amount of AQP4 expression in periarterial, perivenous, and pericapillary endfeet. Whereas perivenous and pericapillary endfeet did not differ in AQP4 expression, periarterial endfeet exhibited significantly less AQP4 immunoreactivity ([fig. S7, A to C](#)). When non-endfoot AQP4 expression around arteries and veins was compared to expression around capillaries, reduced periarterial expression was clear ([fig. S7, A, B, and D](#)). This effect was largely due to a subpopulation of penetrating arteries that exhibited sharply diminished AQP4 immunoreactivity ([fig. S7, A and D](#)).

### Astroglial water transport facilitates bulk ISF solute clearance from the parenchyma

These data demonstrate that astroglial water flux facilitates the movement of subarachnoid CSF into and through the brain interstitium. One possible function for this transparenchymal CSF flux is the clearance of fluid and solutes from the brain interstitium. We tested this by examining the effect of *Aqp4* gene deletion upon the clearance of radiolabeled [ $^3\text{H}$ ]mannitol from the brain parenchyma ([fig. S8A](#)). In *Aqp4*-null mice, [ $^3\text{H}$ ]mannitol clearance from the brain interstitium was reduced by ~70% compared to that of wild-type animals ([Fig. 5A](#)). In wild-type mice, the rate of clearance for [ $^3\text{H}$ ]dextran-10 (with a 55-fold larger molecular size than mannitol) was identical to that of [ $^3\text{H}$ ]mannitol ([fig. S8B](#)), confirming that bulk ISF flow rather than diffusion is responsible for the clearance of these interstitial-delivered tracers ([4, 9](#)). The clearance of [ $^3\text{H}$ ]dextran-10 was also significantly reduced in *Aqp4*-nullmice ([fig. S8B](#)). Our analysis moves beyond the early work of Cserr *et al.* ([4](#)), demonstrating that astroglial AQP4 supports the bulk ISF flow that drives the clearance of interstitial solutes from the brain parenchyma.

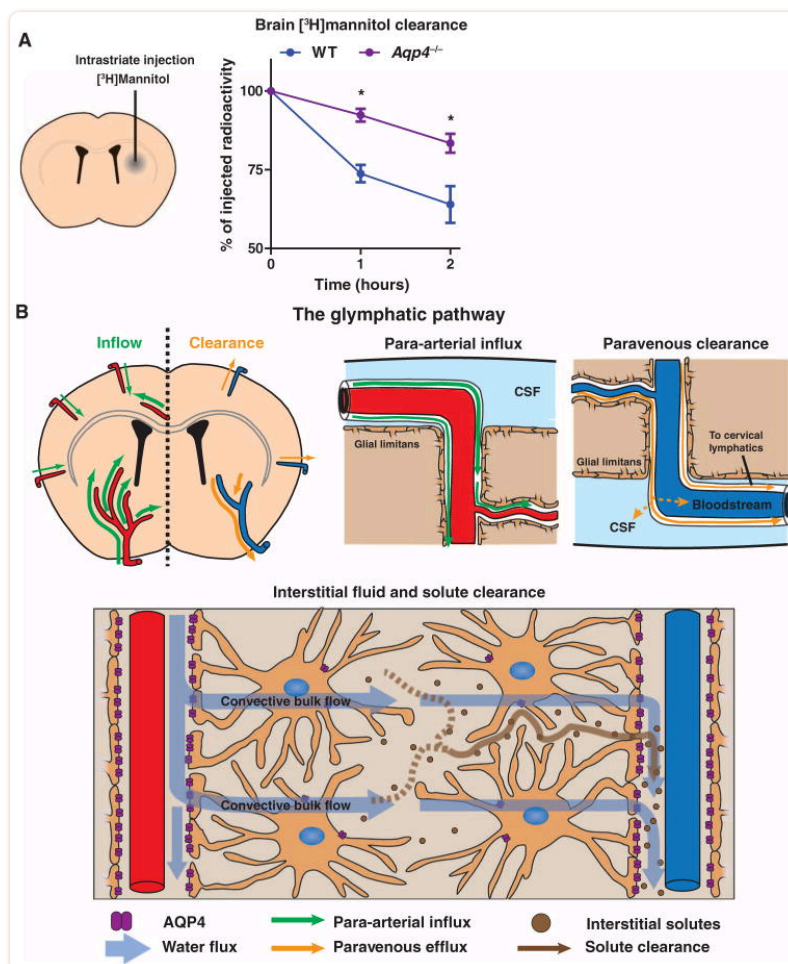


Fig. 5

The glymphatic system supports interstitial solute and fluid clearance from the brain. (A) To evaluate the role of the clearance of interstitial solutes, we measured the elimination of intrastriate [ $^3\text{H}$ ]mannitol from the brain (for details, see [fig. S8A](#)). Over the first 2 hours after injection, the clearance of intrastriate [ $^3\text{H}$ ]mannitol from *Aqp4*-null mouse brains was significantly reduced ( $*P < 0.01$ ,  $n = 4$  per time point) compared to WT controls. (B) Schematic depiction of the glymphatic pathway. In this brain-wide pathway, CSF enters the brain along para-arterial routes, whereas ISF is cleared from the brain along paravenous routes. Convective bulk ISF flow between these influx and clearance routes is facilitated by AQP4-dependent astroglial water flux and drives the clearance of interstitial solutes and fluid from the brain parenchyma. From here, solutes and fluid may be dispersed into the subarachnoid CSF, enter the bloodstream across the postcapillary vasculature, or follow the walls of the draining veins to reach the cervical lymphatics.

### AQP4 facilitates the para-vascular clearance of interstitial amyloid $\beta$

Soluble amyloid  $\beta$  (A $\beta$ ) is present in the interstitium of the healthy young brain, yet interstitial A $\beta$  levels are correlated with amyloid plaque burden (18). We thus evaluated whether AQP4-dependent ISF bulk flow contributes to the clearance of soluble A $\beta$  from the brain. After intrastratial injection of  $^{125}\text{I}$ -amyloid  $\beta_{1-40}$ , the compound was rapidly cleared from the brain ([Fig. 6A](#)). In agreement with the receptor-mediated efflux of A $\beta$  across the BBB (19), the rate of  $^{125}\text{I}$ -amyloid  $\beta_{1-40}$  clearance from the brain exceeded that of either [ $^3\text{H}$ ]mannitol or [ $^3\text{H}$ ]dextran-10, which lacks specific efflux receptors ([fig. S8](#)). In *Aqp4*-null mice, the rate of  $^{125}\text{I}$ -amyloid  $\beta_{1-40}$  clearance was reduced by ~55% ([Fig. 6A](#)) compared to that of wild-type controls. This suggests that a large proportion of soluble A $\beta$  is removed by

bulk flow along the gliovascular clearance system rather than locally across the BBB. In support of this conclusion, we found that fluorescent-tagged A $\beta$  moved rapidly along the vasculature when injected in the striatum, accumulating along the microvasculature and large-caliber internal cerebral and caudal rhinal veins (Fig. 6, B to D).

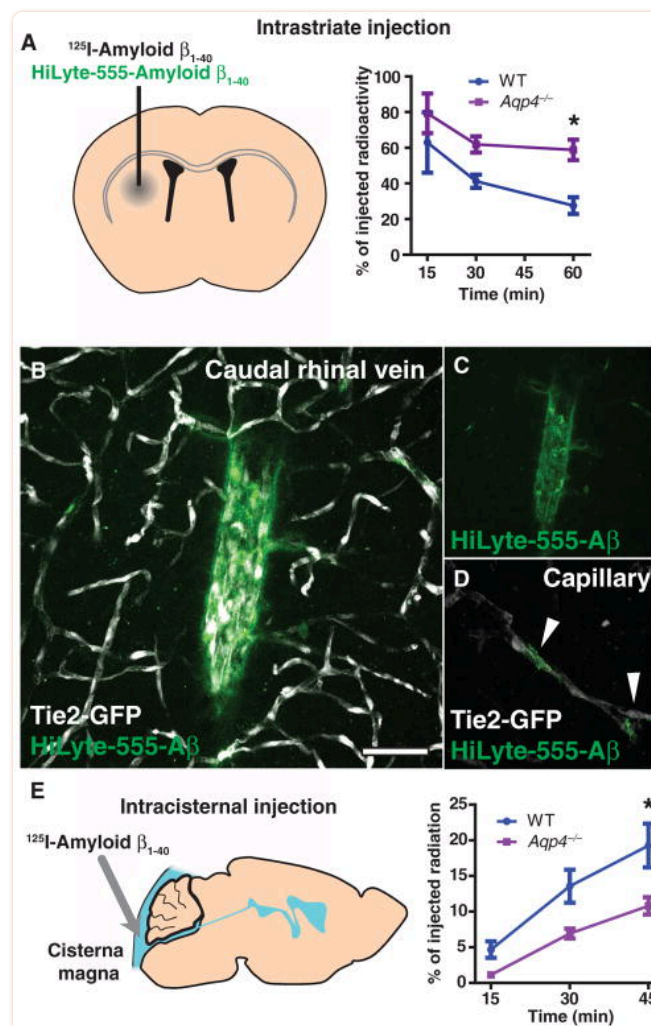


Fig. 6

Interstitial A $\beta$  is cleared along paravascular pathways. To evaluate whether interstitial soluble amyloid A $\beta$  is cleared along the same pathways as other tracers, we injected fluorescent or radiolabeled amyloid  $\beta_{1-40}$  into the mouse striatum. (A) Fifteen minutes, 30 min, or 1 hour after  $^{125}\text{I}$ -amyloid  $\beta_{1-40}$  injection, whole-brain radiation was measured, as detailed in fig. S8. At  $t = 60$  min in WT animals,  $^{125}\text{I}$ -amyloid  $\beta_{1-40}$  was cleared more rapidly than [ $^3\text{H}$ ]mannitol or [ $^3\text{H}$ ]dextran-10.  $^{125}\text{I}$ -Amyloid  $\beta_{1-40}$  clearance in  $Aqp4$ -null mice was significantly reduced ( $*P < 0.05$ ,  $n = 4$  to 6 per time point). (B to D) One hour after injection with HyLyte-555-amyloid  $\beta_{1-40}$  into Tie2-GFP mice, tracer accumulated along capillaries (D, arrows) and large draining veins (B and C). Image in (C) depicts (B) without the endothelial GFP fluorescence signal. (E) To evaluate whether soluble A $\beta$  within the CSF could recycle through the brain parenchyma, we injected  $^{125}\text{I}$ -amyloid  $\beta_{1-40}$  intracisternally, and we evaluated radiotracer influx into the brain (as in fig. S2) 15, 30, and 45 min after injection.  $^{125}\text{I}$ -Amyloid  $\beta_{1-40}$  entered the brain in a manner comparable to [ $^3\text{H}$ ]dextran-10, and compared to WT controls,  $^{125}\text{I}$ -amyloid  $\beta_{1-40}$  influx was significantly reduced in  $Aqp4$ -null mice ( $*P < 0.05$ ,  $n = 4$  to 6 per time point). Scale bar, 50  $\mu\text{m}$ .

Soluble A $\beta$  is also present in the CSF, from which it may be cleared by transport across the choroid plexus (20), as well as by bulk CSF turnover (21). We thus asked whether soluble A $\beta_{1-40}$  within the CSF compartment recirculates through the brain parenchyma. After intracisternal  $^{125}\text{I}$ -amyloid  $\beta_{1-40}$  injection, brain  $^{125}\text{I}$ -amyloid  $\beta_{1-40}$  levels increased in a manner comparable to [ $^3\text{H}$ ]dextran-10 (Fig. 6E, compare to Fig. 1O). In the *Aqp4*-null mouse, bulk influx of  $^{125}\text{I}$ -amyloid  $\beta_{1-40}$  was significantly reduced compared to wild types (Fig. 6E). These data suggest that although interstitial soluble A $\beta$  is cleared along the gliovascular pathway, a portion of A $\beta$  within the CSF compartment may recirculate through the brain along this same route.

## DISCUSSION

---

We have identified a brain-wide pathway for fluid transport in mice, which includes the para-arterial influx of subarachnoid CSF into the brain interstitium, followed by the clearance of ISF along large-caliber draining veins. Interstitial bulk flow between these influx and efflux pathways depends upon trans-astrocytic water movement, and the continuous movement of fluid through this system is a critical contributor to the clearance of interstitial solutes, likely including soluble A $\beta_{1-40}$ , from the brain. In light of its dependence on glial water flux, and its subservience of a lymphatic function in interstitial solute clearance, we propose that this system be called the “glymphatic” pathway (Fig. 5B and fig. S9).

The relationship between the CSF compartment and the peripheral lymphatics is well established (8). In mammals, ~50% of radiolabeled albumin injected into the CSF drains to the cervical lymphatics via the cribriform plate, whereas the remainder is cleared to the bloodstream via arachnoid granulations of the dural sinuses (22–24). These recognized patterns of drainage initially led to the concept that CSF serves a “lymphatic” function through its exchange with brain ISF along paravascular spaces (6, 25). Consistent with our findings reported here, studies in the rat demonstrated that as much as 75% of tracer injected into the brain interstitium was cleared to the subarachnoid CSF, accounting for about 11% of total CSF production (26). Our identification of paravenous pathways, particularly those surrounding the medial internal cerebral and caudal rhinal veins, as the primary route for clearance is in contrast to some studies identifying para-arterial sheaths as pathways for tracer clearance (26, 27). We surmise that this para-arterial labeling after intraparenchymal injections is largely an artifact of high local intraparenchymal pressure from the injection and does not reflect the natural pathway for solute efflux. We observed that with intraparenchymal injections, para-arterial spaces accumulated tracer close to the injection site. If observations are limited to these sites, then it might mistakenly be concluded that tracer efflux is occurring primarily along para-arterial efflux pathways. However, at locations most remote from the injection site, tracer accumulation was greatest surrounding large-caliber draining veins (Fig. 3H and fig. S5E).

Our results confirm, in part, the basic observations of Rennels *et al.* (15, 28) in which horseradish peroxidase (molecular size, 40 kD) injected into subarachnoid space at the cisterna magna in the cat moved rapidly into the brain along para-arterial pathways. These findings were rebutted by Cserr and colleagues, who concluded that paravascular influx of subarachnoid CSF was “slow and variable in direction” (11, 29). Our present findings, including in vivo two-photon imaging (Fig. 2, fig. S3, and movie S1), ex vivo analysis with double-transgenic reporter mice (Figs. 1 and 3 and figs. S4 and S5), and quantitative radiotracer experiments (Fig. 1O), refute this conclusion. One possible reason for these discrepant findings is the previous studies’ choice of larger-molecular weight tracers. Our in vivo (Fig. 2, B to E, and fig. S3) and ex vivo (Fig. 2N) imaging, as well as radiotracer influx data (Fig. 1O), demonstrate that tracer influx from the subarachnoid space into the brain parenchyma is dependent upon molecular weight. In previous studies evaluating the movement of subarachnoid CSF into the



brain parenchyma, inulin (molecular size, ~5kD), albumin (molecular size, 66 kD), and dextrans (usually 2000 kD) are typically used as CSF tracers ([3](#), [10](#), [11](#), [29](#)). On the basis of our findings, these studies underestimated the extent and rate of subarachnoid CSF influx into the brain interstitium. Other methodological differences appear to be at play as well. Pullen *et al.* used an open ventriculo-cisternal and cisterno-cisternal perfusion method that left the cisternal outflow tube open to the atmosphere for sample collection ([29](#)). Ichimura *et al.* pressure injected tracer directly into the paravascular and subarachnoid space at the site of observation ([11](#)). In our own experiments, we found that when the dura was pierced, as in the methodology used by Cserr and colleagues ([11](#), [29](#)), paravascular tracer flux was virtually abolished, suggesting that the maintenance of the hydraulic integrity of the subarachnoid and paravascular spaces is critical for maintaining paravascular bulk flow.

### Role of AQP4 in paravascular pathway function

Our data suggest that AQP4-dependent astroglial water fluxes couple para-arterial CSF influx to paravenous ISF clearance within the brain. AQP4 has been implicated in water uptake into the brain tissue during the evolution of cytotoxic edema, as well as in water clearance after vasogenic edema ([30](#), [31](#)). Our observations suggest that perivascular AQP4 facilitates the influx of subarachnoid CSF from para-arterial spaces into the brain interstitium, as well as the subsequent clearance of ISF via convective bulk flow ([3](#), [4](#)). We observed bulk flow CSF movement along para-arterial pathways directly using in vivo two-photon imaging of intracisternally injected TR-d3 and FITC-d2000. Both of these agents moved rapidly along the wall of pial arteries to enter the Virchow-Robin spaces without mixing with CSF in the surrounding subarachnoid compartment ([Fig. 2B](#) and [movie S1](#)). Consistent with ultrastructural analyses of leptomeningeal vessels conducted by Weller ([12](#)), this indicates that the paravascular space around surface arteries and the Virchow-Robin space into which these penetrate comprise a physically and functionally distinct subcompartment through which CSF rapidly enters the brain parenchyma by bulk flow. This CSF flux is likely driven by arterial pulsation ([13–15](#)): the directionality of CSF influx into para-arterial spaces perhaps reflecting the differing pulse pressures between para-arterial and paravenous pathways.

Perivascular astrocytic endfeet provide complete coverage of the cerebral microvasculature, with only 20-nm clefts between overlapping processes providing direct communication with the interstitium ([17](#)). This interposes a high-resistance barrier to fluid and solute flux between paravascular and interstitial compartments. AQP4, which occupies ~50% of the surface area of capillary-facing endfeet ([32](#)), constitutes a low-resistance pathway for water movement between these compartments. We speculate that transglial water movement, presumably driven by the hydrostatic pressure of para-arterial bulk flow, drives solute flux from the paravascular space into the interstitium, either via specific astroglial solute transporters or through the intercellular cleft between endfeet. This role for AQP4 is supported by the effect of *Aqp4* gene deletion on the movement of TR-d3 between the paravascular space and the surrounding interstitium. The sieving effect of the endfeet (restricting the movement of solutes as they approach a  $d_H$  of 20 nm) may account for the influence of molecular weight on tracer penetration into the interstitium ([fig. S9](#)).

As subarachnoid CSF enters the interstitium and mixes with ISF, both are cleared together with any associated solutes (including soluble A $\beta$ ) along specific paravenous pathways, including both the internal cerebral and the caudal rhinal veins. These veins drain directly into the great vein of Galen and the straight sinus (internal cerebral vein) and the transverse sinus (caudal rhinal vein) ([33](#)). As with the para-arterial influx route, AQP4 localized to astroglial endfeet around the microvasculature, and these large draining veins provide a low-resistance pathway for water and accompanying solute efflux into the

paravenous compartment. This is consistent with the observation that in *Aqp4*-null animals, bulk flow-dependent clearance of interstitial solutes was reduced by ~70%. We speculate that the relationship between these paravenous spaces and the dural sinuses provides a low pressure sink that, in combination with arterial pulsations within the subarachnoid space, results in an arteriovenous hydrostatic gradient that drives paravascular CSF bulk flow and ISF clearance. In this context, the higher expression of perivascular AQP4 surrounding veins compared to arteries may help to maintain low resistance clearance routes for ISF. This notion is supported by the observation that mice lacking the *Aqp4* gene exhibit an enlarged extracellular space in the brain parenchyma compared to wild-type animals (34), which may represent a compensatory phenomenon to counteract the higher resistance toward parenchymal bulk ISF efflux in these mice. Mice with mislocalized or absent perivascular astrocytic AQP4, including  $\alpha$ -syntrophin (35), *mdx* (36), and *Aqp4* (37) knockout mice, show swollen endfeet and other pathological changes to perivascular astrocytes. These changes, related to the dysregulation of scaffolding at the perivascular endfoot, might account for the observed effects of *Aqp4* gene deletion on interstitial bulk flow and solute clearance. Subsequent electron microscopic studies, however, reported no apparent ultrastructural changes in either the BBB or the perivascular astrocytic endfeet of *Aqp4*-null mice (38, 39), and our own analysis demonstrated that the paravascular space of *Aqp4*-null mice was structurally intact through the depth of the cortex (fig. S6).

Although we demonstrate that interstitial solutes are cleared by AQP4-dependent bulk flow along paravenous pathways, these pathways may not necessarily be the terminal route for solute clearance from the cranium. From previous studies, two routes for such terminal clearance appear most likely. First, the movement of solutes along the microvasculature and large draining veins of the brain provide ready access of solutes to specific transport mechanisms at the BBB. A second possibility is that solutes draining along the internal cerebral and caudal rhinal veins to their associated sinuses are cleared to the bloodstream via arachnoid granulations (22–24), providing an exit route for interstitial solutes that do not interact with or have saturated specific transport pathways at the BBB.

### The paravascular pathway and disease

Our finding that disruption of this pathway in *Aqp4*-null mice resulted in the failure of solute clearance may be of clinical relevance for neurodegenerative diseases in which the mis-accumulation of neurotoxic depositions contributes to disease development. Ball *et al.* have reported that intraparenchymally injected A $\beta$  is cleared along paravascular pathways (40), whereas the failure of paravascular soluble A $\beta$  clearance has been suggested to underlie the formation of extracellular A $\beta$  aggregates and disease progression in Alzheimer's disease (41). We report that fluorescent-tagged soluble A $\beta_{1-40}$  injected into the brain parenchyma is cleared along the same paravascular pathways as other fluorescent tracers and that the clearance of radiolabeled A $\beta_{1-40}$  from the interstitium was substantially reduced in *Aqp4*-null mice. This is intriguing because of the association of Alzheimer's disease with reactive gliosis and the increasing gliosis observed in the aging brain (42–44). Altered AQP4 expression and localization in reactive astrocytes under neuropathological conditions (45) may contribute to deranged interstitial bulk flow and a resulting failure in the clearance of neurotoxic solutes such as A $\beta$ .

Soluble A $\beta_{1-40}$  was cleared from the brain interstitium more rapidly than a comparably sized dextran molecule, suggesting that interaction between specific BBB A $\beta$  efflux receptors with bulk flow-dependent clearance (46, 47) may occur. The clearance of A $\beta$  along specific anatomical paravascular pathways (including the deep venous system) raises the possibility that transendothelial A $\beta$  efflux may not be uniform throughout the brain vasculature but may occur at certain specialized clearance vessels. Soluble A $\beta$  moving along paravenous clearance pathways reenters the CSF compartment, either within

the ventricles (internal cerebral veins) or in the subarachnoid space (caudal rhinal veins). The ventricular pathway provides a direct route to the choroid plexus, a structure that may contribute to A $\beta$  clearance from the CSF compartment (48). A $\beta$  sequestered from the aqueous phase into plaques (primarily A $\beta_{1-42}$ ) would not be cleared by bulk flow either to remote sites of transendothelial or choroidal efflux, or by bulk clearance via the CSF.

These patterns of parenchymal fluid flow suggest a number of therapeutic possibilities. First, improving the efficiency of AQP4-dependent bulk flow might permit the improved clearance of soluble A $\beta$ , potentially accelerating either its degradation or its re-uptake into the systemic circulation. Conversely, impeding solute clearance could slow the removal of therapeutic agents, such as antineoplastic agents and immune modulators, from the brain. AQP4-dependent bulk flow could facilitate immune surveillance of the brain parenchyma without compromising CNS immune privilege. Both lymphocytes and antigen-presenting cells in the subarachnoid CSF (49) may detect interstitial antigens delivered to the CSF by paravenous bulk outflow. Indeed, *Aqp4*-null mice exhibit reduced neuroinflammation after intracerebral lipopolysaccharide injection (50). This attenuation of the peripheral immune response could be a consequence of reduced antigen accumulation in the subarachnoid CSF compartment in *Aqp4*-null mice. These paravascular routes could also serve as pathways for migrating cells and their guidance molecules, thus representing a potential avenue for tumor cell migration (51). Additionally, paravascular routes may be conduits for cell migration, molecularly distinct and functionally overlapping with the perivascular niches for cell genesis and migration in the adult brain parenchyma (52).

Although this pathway is important to fluid and solute homeostasis in the rodent brain, it may even be of greater importance for interstitial solute clearance in humans. One of the hallmarks of bulk flow, compared to simple diffusion, is the independence of solute movement from molecular size (4, 46), because all solutes are carried along with the moving medium at the same rate of fluid flow. In contrast, in simple diffusion, because of the dependence of diffusion rates on molecular size, larger solutes require longer times to clear from the brain parenchyma into the nearest CSF compartment (16, 46). Thus, whereas urea (molecular size, 60 daltons) requires 5.4 hours to diffuse 1 cm within the brain, albumin (molecular size, 66.5 kD) would require 109 hours. On the basis of these values, Cserr postulated that the larger the brain, the greater the dependence upon bulk flow for the efficient clearance of interstitial solutes, particularly for larger molecules such as peptides and proteins that cannot effectively clear via diffusion (16). Thus, in the human brain, paravascular pathways and AQP4-dependent bulk flow may be substantially more critical to brain function than in the rodent brain. To evaluate this possibility, less invasive approaches than those used here for assessing interstitial solute movement in humans, such as magnetic resonance perfusion imaging, will be necessary.

## MATERIALS AND METHODS

---

### Animals

All experiments were approved by the University Committee on Animal Resources of the University of Rochester Medical Center. Unless otherwise noted, we used 8- to 12-week-old male C57BL/6 mice (Charles River). FVB/N-Tg(GFAPGFP)14Mes/J (GFAP-GFP, JAX) mice were used to visualize perivascular astrocytic endfeet. NG2-DsRed and Tie2-GFP:NG2-DsRed were used to identify arteries/arterioles versus veins/venules by endogenous fluorescence: Arteries and arterioles express endothelial GFP and vascular smooth muscle DsRed, and veins and venules express endothelial GFP but lack vascular smooth muscle DsRed. *Aqp4*<sup>-/-</sup> (*Aqp4*-null) mice were generated as described (53).

## Anesthesia

In all experiments, animals were anesthetized with a combination of ketamine (0.12 mg/g intraperitoneally) and xylazine (0.01 mg/g intraperitoneally).

## Experimental procedures

Detailed methods are described in the [Supplementary Methods](#).

## Statistics

In all figures, data are presented as means  $\pm$  SEM. All statistics were performed with the software Prism (GraphPad). A  $P$  value of  $<0.05$  was considered significant. The statistical treatment of each data set is described individually in the [Supplementary Materials](#).

## Supplementary Material

---

### Supplementary Data

Fig. S1. Quantification of fluorescent CSF tracer distribution within the brain parenchyma.

Fig. S2. Measurement of subarachnoid CSF entry into the brain parenchyma.

Fig. S3. In vivo imaging of para-arterial influx of small- and large-molecular weight tracers.

Fig. S4. CSF does not enter the brain parenchyma along paravenous pathways.

Fig. S5. Intracisternally and intraparenchymally injected tracer shares the same paravenous drainage pathway.

Fig. S6. Visualization of paravascular accumulation of tracer and the Virchow-Robin space in wild-type and *Aqp4*-null mice.

Fig. S7. Differential expression of AQP4 in periarterial versus perivenous astrocytes.

Fig. S8. Measurement of interstitial solute clearance from the brain.

Fig. S9. Schematic diagram of paravascular and interstitial bulk flow pathways.

Movie S1. Direct visualization of para-arterial influx of subarachnoid CSF tracer into the brain parenchyma.

Movie S2. Animation depicting the role of paravascular CSF influx in interstitial solute clearance from the brain.

[Click here to view](#).<sup>(3.8M, pdf)</sup>



## Acknowledgments

---

We thank C. Nicholson and G. Dienel for valuable comments on the manuscript and O. P. Ottersen for providing the *Aqp4* knockout mice.

**Funding:** This work was supported by the NIH, the United States Department of Defense, and the Harold and Leila Y. Mathers Charitable Foundation.

## Footnotes

---

**Author contributions:** J.J.I. planned and carried out the experiments, analyzed the data, generated the figures, and wrote the manuscript. M.W., Y.L., B.A.P., W.P., and G.A.G. carried out the experiments and analyzed the data. E.A.N., R.D., G.E.V., S.A.G., and H.B. planned the experiments, analyzed the data, and provided editorial assistance in preparing the manuscript. M.N. planned the experiments and wrote the manuscript.

**Competing interests:** The authors declare that they have no competing interests.

## REFERENCES AND NOTES

---

1. Aukland K, Reed RK. Interstitial-lymphatic mechanisms in the control of extracellular fluid volume. *Physiol Rev.* 1993;73:1–78. [[PubMed](#)] [[Google Scholar](#)]
2. Schmid-Schönbein GW. Microlymphatics and lymph flow. *Physiol Rev.* 1990;70:987–1028. [[PubMed](#)] [[Google Scholar](#)]
3. Abbott NJ. Evidence for bulk flow of brain interstitial fluid: Significance for physiology and pathology. *Neurochem Int.* 2004;45:545–552. [[PubMed](#)] [[Google Scholar](#)]
4. Cserr HF, Cooper DN, Suri PK, Patlak CS. Efflux of radiolabeled polyethylene glycols and albumin from rat brain. *Am J Physiol.* 1981;240:F319–F328. [[PubMed](#)] [[Google Scholar](#)]
5. Cserr HF, Harling-Berg CJ, Knopf PM. Drainage of brain extracellular fluid into blood and deep cervical lymph and its immunological significance. *Brain Pathol.* 1992;2:269–276. [[PubMed](#)] [[Google Scholar](#)]
6. Flexner LB. Some problems of the origin, circulation and absorption of the cerebrospinal fluid. *Q Rev Biol.* 1933;8:397–422. [[Google Scholar](#)]
7. Praetorius J. Water and solute secretion by the choroid plexus. *Pflugers Arch.* 2007;454:1–18. [[PubMed](#)] [[Google Scholar](#)]
8. Koh L, Zakharov A, Johnston M. Integration of the subarachnoid space and lymphatics: Is it time to embrace a new concept of cerebrospinal fluid absorption? *Cerebrospinal Fluid Res.* 2005;2:6. [[PMC free article](#)] [[PubMed](#)] [[Google Scholar](#)]
9. Syková E, Nicholson C. Diffusion in brain extracellular space. *Physiol Rev.* 2008;88:1277–1340. [[PMC free article](#)] [[PubMed](#)] [[Google Scholar](#)]
10. Proescholdt MG, Hutto B, Brady LS, Herkenham M. Studies of cerebrospinal fluid flow and penetration into brain following lateral ventricle and cisterna magna injections of the tracer [ $^{14}\text{C}$ ]inulin in rat. *Neuroscience.* 2000;95:577–592. [[PubMed](#)] [[Google Scholar](#)]
11. Ichimura T, Fraser PA, Cserr HF. Distribution of extracellular tracers in perivascular spaces of the rat brain. *Brain Res.* 1991;545:103–113. [[PubMed](#)] [[Google Scholar](#)]

12. Weller RO. Microscopic morphology and histology of the human meninges. *Morphologie*. 2005;89:22–34. [[PubMed](#)] [[Google Scholar](#)]
13. Hadaczek P, Yamashita Y, Mirek H, Tamas L, Bohn MC, Noble C, Park JW, Bankiewicz K. The “perivascular pump” driven by arterial pulsation is a powerful mechanism for the distribution of therapeutic molecules within the brain. *Mol Ther*. 2006;14:69–78. [[PMC free article](#)] [[PubMed](#)] [[Google Scholar](#)]
14. Schley D, Carare-Nnadi R, Please CP, Perry VH, Weller RO. Mechanisms to explain the reverse perivascular transport of solutes out of the brain. *J Theor Biol*. 2006;238:962–974. [[PubMed](#)] [[Google Scholar](#)]
15. Rennels ML, Blaumanis OR, Grady PA. Rapid solute transport throughout the brain via paravascular fluid pathways. *Adv Neurol*. 1990;52:431–439. [[PubMed](#)] [[Google Scholar](#)]
16. Cserr HF. Physiology of the choroid plexus. *Physiol Rev*. 1971;51:273–311. [[PubMed](#)] [[Google Scholar](#)]
17. Mathiisen TM, Lehre KP, Danbolt NC, Ottersen OP. The perivascular astroglial sheath provides a complete covering of the brain microvessels: An electron microscopic 3D reconstruction. *Glia*. 2010;58:1094–1103. [[PubMed](#)] [[Google Scholar](#)]
18. Bero AW, Yan P, Roh JH, Cirrito JR, Stewart FR, Raichle ME, Lee JM, Holtzman DM. Neuronal activity regulates the regional vulnerability to amyloid- $\beta$  deposition. *Nat Neurosci*. 2011;14:750–756. [[PMC free article](#)] [[PubMed](#)] [[Google Scholar](#)]
19. Zlokovic BV, Deane R, Sagare AP, Bell RD, Winkler EA. Low-density lipoprotein receptor-related protein-1: A serial clearance homeostatic mechanism controlling Alzheimer’s amyloid  $\beta$ -peptide elimination from the brain. *J Neurochem*. 2010;115:1077–1089. [[PMC free article](#)] [[PubMed](#)] [[Google Scholar](#)]
20. Crossgrove JS, Li GJ, Zheng W. The choroid plexus removes  $\beta$ -amyloid from brain cerebrospinal fluid. *Exp Biol Med*. 2005;230:771–776. [[PMC free article](#)] [[PubMed](#)] [[Google Scholar](#)]
21. Serot JM, Zmudka J, Jouanny P. A possible role for CSF turnover and choroid plexus in the pathogenesis of late onset Alzheimer’s disease. *J Alzheimers Dis*. 2012;30:17–26. [[PubMed](#)] [[Google Scholar](#)]
22. Bradbury MW, Westrop RJ. Factors influencing exit of substances from cerebrospinal fluid into deep cervical lymph of the rabbit. *J Physiol*. 1983;339:519–534. [[PMC free article](#)] [[PubMed](#)] [[Google Scholar](#)]
23. Boulton M, Young A, Hay J, Armstrong D, Flessner M, Schwartz M, Johnston M. Drainage of CSF through lymphatic pathways and arachnoid villi in sheep: Measurement of  $^{125}\text{I}$ -albumin clearance. *Neuropathol Appl Neurobiol*. 1996;22:325–333. [[PubMed](#)] [[Google Scholar](#)]
24. Johnston M, Zakharov A, Papaiconomou C, Salmasi G, Armstrong D. Evidence of connections between cerebrospinal fluid and nasal lymphatic vessels in humans, non-human primates and other mammalian species. *Cerebrospinal Fluid Res*. 2004;1:2. [[PMC free article](#)] [[PubMed](#)] [[Google Scholar](#)]
25. Weed LH. The absorption of cerebrospinal fluid into the venous system. *Am J Anat*. 1923;31:191–221. [[Google Scholar](#)]
26. Szentistványi I, Patlak CS, Ellis RA, Cserr HF. Drainage of interstitial fluid from different regions of rat brain. *Am J Physiol*. 1984;246:F835–F844. [[PubMed](#)] [[Google Scholar](#)]
27. Carare RO, Bernardes-Silva M, Newman TA, Page AM, Nicoll JA, Perry VH, Weller RO. Solutes, but not cells, drain from the brain parenchyma along basement membranes of capillaries and arteries: Significance for cerebral amyloid angiopathy and neuroimmunology. *Neuropathol Appl Neurobiol*. 2008;34:131–144. [[PubMed](#)] [[Google Scholar](#)]
28. Rennels ML, Gregory TF, Blaumanis OR, Fujimoto K, Grady PA. Evidence for a ‘paravascular’ fluid circulation in the mammalian central nervous system, provided by the rapid distribution of tracer protein throughout the brain from the subarachnoid space. *Brain Res*. 1985;326:47–63. [[PubMed](#)] [[Google Scholar](#)]

29. Pullen RG, DePasquale M, Cserr HF. Bulk flow of cerebrospinal fluid into brain in response to acute hyperosmolality. *Am J Physiol*. 1987;253:F538–F545. [[PubMed](#)] [[Google Scholar](#)]
30. Papadopoulos MC, Verkman AS. Aquaporin-4 and brain edema. *Pediatr Nephrol*. 2007;22:778–784. [[PMC free article](#)] [[PubMed](#)] [[Google Scholar](#)]
31. Haj-Yasein NN, Vindedal GF, Eilert-Olsen M, Gundersen GA, Skare Ø, Laake P, Klungland A, Thorén AE, Burkhardt JM, Ottersen OP, Nagelhus EA. Glial-conditional deletion of aquaporin-4 (*Aqp4*) reduces blood–brain water uptake and confers barrier function on perivascular astrocyte endfeet. *Proc Natl Acad Sci USA*. 2011;108:17815–17820. [[PMC free article](#)] [[PubMed](#)] [[Google Scholar](#)]
32. Nielsen S, Nagelhus EA, Amiry-Moghaddam M, Bourque C, Agre P, Ottersen OP. Specialized membrane domains for water transport in glial cells: High-resolution immunogold cytochemistry of aquaporin-4 in rat brain. *J Neurosci*. 1997;17:171–180. [[PMC free article](#)] [[PubMed](#)] [[Google Scholar](#)]
33. Dorr A, Sled JG, Kabani N. Three-dimensional cerebral vasculature of the CBA mouse brain: A magnetic resonance imaging and micro computed tomography study. *Neuroimage*. 2007;35:1409–1423. [[PubMed](#)] [[Google Scholar](#)]
34. Yao X, Hrabetová S, Nicholson C, Manley GT. Aquaporin-4-deficient mice have increased extracellular space without tortuosity change. *J Neurosci*. 2008;28:5460–5464. [[PMC free article](#)] [[PubMed](#)] [[Google Scholar](#)]
35. Amiry-Moghaddam M, Otsuka T, Hurn PD, Traystman RJ, Haug FM, Froehner SC, Adams ME, Neely JD, Agre P, Ottersen OP, Bhardwaj A. An  $\alpha$ -syntrophin-dependent pool of AQP4 in astroglial end-feet confers bidirectional water flow between blood and brain. *Proc Natl Acad Sci USA*. 2003;100:2106–2111. [[PMC free article](#)] [[PubMed](#)] [[Google Scholar](#)]
36. Frigeri A, Nicchia GP, Nico B, Quondamatteo F, Herken R, Roncali L, Svelto M. Aquaporin-4 deficiency in skeletal muscle and brain of dystrophic mdx mice. *FASEB J*. 2001;15:90–98. [[PubMed](#)] [[Google Scholar](#)]
37. Zhou J, Kong H, Hua X, Xiao M, Ding J, Hu G. Altered blood-brain barrier integrity in adult aquaporin-4 knockout mice. *Neuroreport*. 2008;19:1–5. [[PubMed](#)] [[Google Scholar](#)]
38. Eilert-Olsen M, Haj-Yasein NN, Vindedal GF, Enger R, Gundersen GA, Hoddevik EH, Petersen PH, Haug FM, Skare Ø, Adams ME, Froehner SC, Burkhardt JM, Thoren AE, Nagelhus EA. Deletion of aquaporin-4 changes the perivascular glial protein scaffold without disrupting the brain endothelial barrier. *Glia*. 2012;60:432–440. [[PubMed](#)] [[Google Scholar](#)]
39. Saadoun S, Tait MJ, Reza A, Davies DC, Bell BA, Verkman AS, Papadopoulos MC. AQP4 gene deletion in mice does not alter blood–brain barrier integrity or brain morphology. *Neuroscience*. 2009;161:764–772. [[PubMed](#)] [[Google Scholar](#)]
40. Ball KK, Cruz NF, Mrak RE, Dienel GA. Trafficking of glucose, lactate, and amyloid- $\beta$  from the inferior colliculus through perivascular routes. *J Cereb Blood Flow Metab*. 2010;30:162–176. [[PMC free article](#)] [[PubMed](#)] [[Google Scholar](#)]
41. Weller RO, Subash M, Preston SD, Mazanti I, Carare RO. Perivascular drainage of amyloid- $\beta$  peptides from the brain and its failure in cerebral amyloid angiopathy and Alzheimer’s disease. *Brain Pathol*. 2008;18:253–266. [[PMC free article](#)] [[PubMed](#)] [[Google Scholar](#)]
42. Ross GW, O’Callaghan JP, Sharp DS, Petrovitch H, Miller DB, Abbott RD, Nelson J, Launer LJ, Foley DJ, Burchfiel CM, Hardman J, White LR. Quantification of regional glial fibrillary acidic protein levels in Alzheimer’s disease. *Acta Neurol Scand*. 2003;107:318–323. [[PubMed](#)] [[Google Scholar](#)]
43. O’Callaghan JP, Miller DB. The concentration of glial fibrillary acidic protein increases with age in the mouse and rat brain. *Neurobiol Aging*. 1991;12:171–174. [[PubMed](#)] [[Google Scholar](#)]
44. Verkhratsky A, Parpura V. Recent advances in (patho)physiology of astroglia. *Acta Pharmacol Sin*. 2010;31:1044–1054. [[PMC free article](#)] [[PubMed](#)] [[Google Scholar](#)]

45. Hamby ME, Sofroniew MV. Reactive astrocytes as therapeutic targets for CNS disorders. *Neurotherapeutics*. 2010;7:494–506. [[PMC free article](#)] [[PubMed](#)] [[Google Scholar](#)]
46. Groothuis DR, Vavra MW, Schlageter KE, Kang EW, Itskovich AC, Hertzler S, Allen CV, Lipton HL. Efflux of drugs and solutes from brain: The interactive roles of diffusional transcapillary transport, bulk flow and capillary transporters. *J Cereb Blood Flow Metab*. 2007;27:43–56. [[PubMed](#)] [[Google Scholar](#)]
47. Deane R, Bell RD, Sagare A, Zlokovic BV. Clearance of amyloid- $\beta$  peptide across the blood-brain barrier: Implication for therapies in Alzheimer's disease. *CNS Neurol Disord Drug Targets*. 2009;8:16–30. [[PMC free article](#)] [[PubMed](#)] [[Google Scholar](#)]
48. Alvira-Botero X, Carro EM. Clearance of amyloid- $\beta$  peptide across the choroid plexus in Alzheimer's disease. *Curr Aging Sci*. 2010;3:219–229. [[PubMed](#)] [[Google Scholar](#)]
49. Ransohoff RM, Kivisäkk P, Kidd G. Three or more routes for leukocyte migration into the central nervous system. *Nat Rev Immunol*. 2003;3:569–581. [[PubMed](#)] [[Google Scholar](#)]
50. Li L, Zhang H, Varrin-Doyer M, Zamvil SS, Verkman AS. Proinflammatory role of aquaporin-4 in autoimmune neuroinflammation. *FASEB J*. 2011;25:1556–1566. [[PMC free article](#)] [[PubMed](#)] [[Google Scholar](#)]
51. Kienast Y, von Baumgarten L, Fuhrmann M, Klinkert WE, Goldbrunner R, Herms J, Winkler F. Real-time imaging reveals the single steps of brain metastasis formation. *Nat Med*. 2010;16:116–122. [[PubMed](#)] [[Google Scholar](#)]
52. Goldman SA, Chen Z. Perivascular instruction of cell genesis and fate in the adult brain. *Nat Neurosci*. 2011;14:1382–1389. [[PMC free article](#)] [[PubMed](#)] [[Google Scholar](#)]
53. Thrane AS, Rappold PM, Fujita T, Torres A, Bekar LK, Takano T, Peng W, Wang F, Thrane VR, Enger R, Haj-Yasein NN, Skare Ø, Holen T, Klungland A, Ottersen OP, Nedergaard M, Nagelhus EA. Critical role of aquaporin-4 (AQP4) in astrocytic  $\text{Ca}^{2+}$  signaling events elicited by cerebral edema. *Proc Natl Acad Sci USA*. 2011;108:846–851. [[PMC free article](#)] [[PubMed](#)] [[Google Scholar](#)]
54. Zhu X, Bergles DE, Nishiyama A. NG2 cells generate both oligodendrocytes and gray matter astrocytes. *Development*. 2008;135:145–157. [[PubMed](#)] [[Google Scholar](#)]
55. Takano T, Tian GF, Peng W, Lou N, Libionka W, Han X, Nedergaard M. Astrocyte-mediated control of cerebral blood flow. *Nat Neurosci*. 2006;9:260–267. [[PubMed](#)] [[Google Scholar](#)]
56. Lehre KP, Levy LM, Ottersen OP, Storm-Mathisen J, Danbolt NC. Differential expression of two glial glutamate transporters in the rat brain: Quantitative and immunocytochemical observations. *J Neurosci*. 1995;15:1835–1853. [[PMC free article](#)] [[PubMed](#)] [[Google Scholar](#)]